J Biol Inorg Chem (2001) 6: 791–800
DOI 10.1007/s007750100255

ORIGINAL ARTICLE

J.M. Rebelo · J.M. Dias · R. Huber
J.J.G. Moura · M.J. Romão

Structure refinement of the aldehyde oxidoreductase from *Desulfovibrio gigas* (MOP) at 1.28 Å

Received: 9 January 2001 / Accepted: 2 May 2001 / Published online: 14 June 2001

Abstract The sulfate-reducing bacterium aldehyde oxidoreductase from *Desulfovibrio gigas* (MOP) is a member of the xanthine oxidase family of enzymes. It has 907 residues on a single polypeptide chain, a molybdopterin cytosine dinucleotide (MCD) cofactor and two [2Fe-2S] iron-sulfur clusters. Synchrotron data to almost atomic resolution were collected for improved cryo-cooled crystals of this enzyme in the oxidized form. The cell constants of $a = b = 141.78$ Å and $c = 160.87$ Å are about 2% shorter than those of room temperature data, yielding 233,755 unique reflections in space group $P6_122$, at 1.28 Å resolution. Throughout the entire refinement the full gradient least-squares method was used, leading to a final R factor of 14.5 and R_{free} factor of 19.3 (4σ cut-off) with "riding" H-atoms at their calculated positions. The model contains 8146 non-hydrogen atoms described by anisotropic displacement parameters with an observations/parameters ratio of 4.4. It includes alternate conformations for 17 amino acid residues. At 1.28 Å resolution, three Cl^- and two Mg^{2+} ions from the crystallization solution were clearly identified. With the exception of one Cl^- which is buried and 8 Å distant from the Mo atom, the other ions are close to the molecular surface and may contribute to crystal packing. The overall structure has not changed in comparison to the lower resolution model apart from local corrections that included some loop adjustments and alternate side-chain conformations. Based on the estimated errors of bond distances obtained by blocked least-squares matrix inversion, a more detailed analysis of the three redox centres was possible. For the MCD cofactor, the resulting geometric parameters confirmed its reduction state as a tetrahydropterin. At the Mo centre, estimated corrections calculated for the Fourier ripples artefact are very small when compared to the experimental associated errors, supporting the suggestion that the fifth ligand is a water molecule rather than a hydroxide. Concerning the two iron-sulfur centres, asymmetry in the Fe-S distances as well as differences in the pattern of NH···S hydrogen-bonding interactions was observed, which influences the electron distribution upon reduction and causes non-equivalence of the individual Fe atoms in each cluster.

Keywords High-resolution structure · Xanthine oxidase · Molybdopterin · Aldehyde oxidoreductase · *Desulfovibrio gigas*

Abbreviations *ADPs*: anisotropic displacement parameters · *CGLS*: conjugated gradient least squares · *FFT*: fast Fourier transform · *IPP*: isopropanol · *MCD*: molybdopterin cytosine dinucleotide · *Moco*: pyranopterin-ene-1,2-dithiolate cofactor or molybdopterin zcofactor · *MOD*: aldehyde oxidoreductase from *Desulfovibrio desulfuricans* ATCC 27774 · *MOP*: aldehyde oxidoreductase from *Desulfovibrio gigas*

Introduction

Molybdenum-containing enzymes are a wide redox-active class of enzymes associated with several metabolic functions. Molybdenum plays a major role in biological systems and has been found in two distinct forms: a mixed [Fe-Mo-S] metallic cluster, which occurs in nitrogenases [1], and a mononuclear Mo (or W) atom associated with one or two pyranopterin-ene-1,2-dithiolate cofactors (Moco). Moco-containing enzymes, termed molybdenum hydroxylases or oxotransferases, are functionally subdivided into four families on the

J.M. Rebelo · J.M. Dias · J.J.G. Moura · M.J. Romão (✉)
Departamento de Química, CQFB,
Faculdade de Ciencias e Tecnologia,
Universidade Nova de Lisboa,
2825-114 Monte da Caparica, Portugal
E-mail: mromao@dq.fct.unl.pt
Tel.: +351-21-2948310
Fax: +351-21-2948550

R. Huber
Max-Planck-Institut für Biochemie,
82152 Martinsried, Germany

basis of sequence homology, similar spectroscopic properties and environment of the active site [2, 3]. Examples of crystal structures from members of all these families were reported in the past five years: for the DMSO reductase family, a nitrate reductase [4] and three DMSO reductase structures [5, 6, 7]; for the sulfite oxidase family, the structure of sulfite oxidase [8] and the tungsten aldehyde ferredoxin oxidoreductase [9], which constitutes a distinct family of enzymes; for the xanthine oxidase family of Mo enzymes, the first structurally elucidated representative was the aldehyde oxidoreductase from *Desulfovibrio gigas*, MOP [10, 11, 13]. Very recently, the crystal structure of milk xanthine oxidase was described [12]. We now report the MOP structure in greater detail and refined to atomic resolution.

The MOP enzyme acts as an oxo donor to an aldehyde substrate in a two-step one-electron transfer reaction, whose mechanism was proposed on the basis of 1.8 Å crystallographic studies of different functional forms of the enzyme [13]. These studies were further supported by density functional theory calculations, which indicate that the oxygen atom incorporated into the substrate is derived from the Mo-OH/OH_2 ligand [14, 15]. Recently we have also reported the crystal structure from the homologous aldehyde oxidoreductase from *Desulfovibrio desulfuricans* ATCC 27774 (MOD) [16]. Comparison between these two related enzymes revealed, as expected, a very high structure similarity, but allowed us to establish important features such as the docking site of the physiological electron acceptor.

With the help of cryo-cooling techniques and the use of synchrotron radiation we have now extended the resolution of oxidized, improved, MOP crystals to 1.28 Å and allowed refinement of anisotropic atomic parameters [17, 18], owing to the increased ratio of observations to parameters [33]. The novel structural details are of considerable biochemical relevance.

Materials and methods

Crystallization and data collection

Aerobic purification was carried out employing the strategy described by Moura et al. [19, 20]. Subsequent crystallization was achieved by vapour diffusion on sitting drops using a mixture of purified protein in 10 mM Tris.HCl buffer (pH 7.5) and a crystallizing solution of 30% (v/v) isopropanol as precipitant and 0.2 M $MgCl_2$ as additive in 0.2 M HEPES (pH 7.6), following the procedure described by Romão et al. [10] The presence of the $MgCl_2$ (or $CaCl_2$) salts was essential for crystallization and contributes to the high stability of these crystals (see below).

Crystal nucleation and growth up to a size of about 0.6×0.4×0.4 mm takes about 3 weeks at 4 °C. A cryo-protectant harvesting buffer prepared with the crystallization solution enriched in poly(ethylene glycol) 4000 (PEG 4000) at 30% (w/v) was added to the crystals, which were thus stable over 1 month.

For the data collection of one single crystal cryo-cooled at 100 K, two independent sets of frames were collected, one corresponding to the lower and the other to the higher resolution shells. The measurements were made on a MAR 300 imaging plate detector at the BW6 beamline of DESY. The diffraction data were indexed, recorded, integrated and processed using DENZO, scaled and merged with SCALEPACK [21, 22]. Structure factors were then derived from intensities using TRUNCATE from the CCP4 package [23], and a starting X-PLOR formatted file was generated by MTZ2VARIOUS also from CCP4. The total set of 452,521 reflections was processed with anomalous data included, yielding 233,755 unique reflections with an overall R_{sym} of 3.6% (43.6% in the outer shell). Important statistics are summarized in Table 1.

The new cell constants of the cryo-cooled crystals decreased to about 2% in comparison to the previous crystals which were analysed at –17 °C, reflecting a tighter packing, keeping 54% of solvent content as calculated by the Matthews coefficient [24].

Refinement

An initial randomly chosen subset of 5% of the total observations was isolated for cross validation by the R_{free} factor [25]. Refinement started with X-PLOR 3.1 [26], first including only the data below 1.8 Å resolution. The first atomic model used was taken from the previous 1.8 Å refinement [13]. In this first partial model, all redox cofactors, alcohol and water molecules were excluded. After 40 cycles of rigid body refinement, the R and R_{free} factors decreased from 53.6 and 51.9 to 35.2 and 39.5, respectively. At this stage, the

Table 1 Data collection statistics

	All data	First data set High resolution	Second data set Low resolution
Wavelength (Å)	1.0004 Å		
Temperature (K)	100		
Crystal data			
Space group	$P6_122$		
Unit cell parameters (Å)	$a=b=141.78$, $c=160.87$		
V_M/solvent content (%)	54		
Mosaicity	0.27		
Data collection			
Resolution (Å)	25.0 to 1.28	2.50 to 1.28	25.0 to 2.00
Last resolution shell (Å)	1.33 to 1.28	1.32 to 1.28	2.07 to 2.00
Number of observations	1,896,565	1,487,183	409,494
Number unique reflections	235,491	202,106	62,795
R_{merge} (%)	5.1	9.1	4.0
Last resolution shell (%)	64.2	64.9	13.1
Completeness (%)	97.4	97.0	97.0
Last resolution shell (%)	93.6	92.5	97.8
$I/\sigma(I)$	12.9	7.5	15.4
Last resolution shell	1.6	1.54	8.84

quality of the electron density maps was good enough to correctly place all cofactors as well as some ordered internal solvent water molecules. The molybdopterin cytosine dinucleotide (MCD) cofactor and both iron-sulfur clusters were included in the atomic model for the subsequent refinements. The geometric and force field parameter sets, implemented by Engh and Huber [27], were applied. As the cofactors were included in the model, it was clear that the MCD would also require guiding target values to avoid distortion (see below). Rigid body refinement was followed by 150 cycles of conjugated gradient Powell minimization [26], which lead to an R_{free} and an R value of 34.7 and 31.1, respectively. An additional 25 cycles of individual restrained isotropic temperature factor refinement decreased the R_{free} and R to 33.9 and 29.9, respectively. Higher resolution data were stepwise included from 1.8 Å to 1.45 Å and finally to 1.28 Å. At each step, some cycles of automated refinement were applied and followed by visual map inspection and model rebuilding in TURBO-FRODO [28]. In each step of the visual inspection, more solvent molecules were included when their density was above 1.85 Å e^{-3} (3σ) on F_o–F_c electron density maps, and when they were within H-bonding distance to acceptor groups. Then an automated bulk solvent model was activated, the X-PLOR bulk solvent correction [26], which allowed all measured low-resolution data to be included, and improved significantly the quality of the electron density maps. At this stage the R factor decreased from 23.7 to 20.7 and the R_{free} from 27.6 to 24.4 on a 2σ cut-off electron density level.

Refinement was continued with SHELX 97-2 [29] and introducing anisotropic atomic displacement parameters (ADPs) described by the symmetric U_{ij} second-rank tensor for all non-hydrogen atoms. This change in the refinement protocol was made because SHELX shows advantages in relation to X-PLOR on high-resolution refinements. It employs conventional Fourier structure factor summations rather than fast Fourier transform (FFT) structure factor summations and allows the anisotropic ADP refinement as well as the ability to refine all positional and thermal displacement parameters simultaneously. Beyond keeping the Engh and Huber [27] geometric restraints, new types of restraints related to U_{ij} refinement were also necessary. The first new set of restraints, working as rigid bond U_{ij} restraints, forced bonded atoms to have the same vibration along the direction of the bond (DELU restraint of SHELXH [29]). A second set of restraints limited the degree of anisotropy (ISOR restraint [29]). The last set was used to avoid sharp variations between adjacent atoms (SIMU restraint [29]).

A refinement algorithm with conjugated gradient least squares (CGLS) [30] and diffuse solvent modelling by Babinet's principle was used throughout the rest of the refinement (Table 2). Single-atom anisotropic refinement, alternate conformation modelling, water occupancy rough refinement by setting the occupancy of some waters to 0.5 on several disordered solvent zones, and finally the automatic placement of non-refined riding H atoms on calculated positions lead to a final R of 14.5 and R_{free} of 19.3. A summary of the most important refinement statistics is presented in Table 2 and final model parameters are summarized in Table 3.

Table 2 Refinement protocol

Working set (95%)	226,751	
Independent cross-validation set (5%)	7004	
XPLOR (CGLS)[a]	R	R_{free}
Resolution range (Å)	24.4	1.80
After molecular replacement	53.6	51.9
Rigid body refinement	35.2	39.5
Cofactor inclusion, atomic coordinate refinement	31.1	34.7
B-factor refinement	29.9	33.9
Model corrections	25.1	29.3
Resolution range (Å)	24.4	1.5
Side chain corrections, water inclusion	24.5	28.7
Resolution range	24.4	1.28
Water inclusion, rotamers correction	23.7	27.6
Bulk solvent correction	20.7	24.4
SHELXL (CGLS)[b]	R	R_{free}
Isotropic refinement	21.1	25.2
Anisotropic refinement	17.3	22.1
Double conformation modeling corrections, more solvent	15.6	20.6
End of refinement (4σ cut-off)	14.5	19.3

[a] 2σ cut-off

[b] 2σ cut-off estimated by linear interpolation between 0 and 4σ cut-off

MCD cofactor target values driven by CSD search

The MCD cofactor structure as analysed below was obtained to almost atomic resolution by crystallographic refinement. However, during this refinement, some structural information was required at early stages and used as a restraint. There are no known small-molecule structures with related or similar structure, excluding the associated cytosine dinucleotide. To overcome this problem, a total of 44 bond-type searches corresponding to all the unique MCD internal bonds were executed on the Cambridge Structural Database (CSD) [31]. Each of these searches produced a histogram of bond distances found among all structures available. The bond distance search pattern for each bond between pairs of atoms within the cofactor also included information about the environments of these pairs of atoms, such as to which atoms the named pair of atoms are bonded, and the number and types of bonds this pair of atoms establishes. For all bonds, many occurrences could be detected, and several histograms reached the stop limit of 600 occurrences imposed to end the search. Following histogram analysis, a standard deviation and a mean value were calculated for each histogram. The mean values were calculated and were subsequently introduced as initial bond distance target values for each of the atomic bonds on the MCD moiety, but as the refinement progressed these restraints were decreased and completely released in the final calculations on which the reported MCD geometry is based.

Results and discussion

Overall quality of the model

The quality of the model now presented was analysed with PROCHECK [32], yielding an overall structure quality measure g-factor of –0.11, close to the mean g-factor value for structures of the same nominal resolution [33]. The Ramachandran plot has 91.6% of the residues in the most favoured regions. Only two residues other than glycine or proline are in disallowed positions, Tyr142 ($\phi = 69°$, $\psi = -37°$) and Leu254 ($\phi = 62°$, $\psi = -68°$), exactly the same two outliers as on the MOD structure [16]. Both residues are very clear in density. Tyr142 is a conserved residue in the xanthine oxidase family and is located on the FeS_I domain on a loop that connects helix III to helix IV. Its hydroxyl group establishes hydrogen-bonding interactions with the amide from Cys137, a ligand from one of the iron atoms, and to the carbonyl group of Pro839, thus defining the loop conformation of helix III to helix IV. Leu254, the second outlier, is also very clear in density and is part of the hydrophobic patch, which surrounds the entrance to the tunnel leading to the active site.

Table 3 Final model parameters and statistics

Non-H atoms		8146
907 amino acids		6844
1 MCD		44
2 [2Fe-2S]		8
Waters		1243
Mg		2
Cl		3
Isopropanol		2
Refinement parameters/statistics (SHELX [29])		
Anisotropic temperature U_{ij} restraints[a]		
	R.m.s.d.	Target σ
DELU	0.012	0.030
ISOR	0.108	0.200
SIMU	0.053	0.274
Restrained goodness of fit		1.4
Total no. of reflections		233,755
No. of restraints		87,737
No. of parameters		73,378
Ratio (observations + restraints)/parameters		4.4
Observations/restraints ratio		3.6
Structure quality statistics		
Estimated average atomic coordinate error (Å)[b]		0.10
Average B_{eq} factor (Å^2)		
Overall		24.7
Protein		21.7
Cofactors		16.0
Solvent		38.9
	R.m.s.	Target σ
Distances (Å)	0.013	0.020
Angles (°)	0.029	0.040
Bonded *B*-factors	3.3	–
Ramachandran (%)		
Allowed		91.6
Generously allowed		8.0
Disallowed		0.4
Overall quality measure (*g*-factor)		–0.11
RSC outliers (%)		2.6
Peptide flips (%)		3.0
R-factor (4σ cutoff)		14.5
All data		15.9
Free *R*-factor (4σ cutoff)		19.3
7004 reflections		21.4

[a]According to definition described in the text
[b]Average error estimated from Luzzatti plot

The final r.m.s.d. values for bond distances and angle distances are 0.013 Å and 0.029 Å, respectively (Table 3). All other stereochemical parameters analysed are within the expected standard uncertainty ranges for a set of very high resolution (0.92–1.20 Å) structures available [33], except for some outliers that occur on low ordered regions of the molecule.

The final bonds and angles error estimates were calculated from a least squares (LS) blocked matrix inversion for the cofactors. In this blocked matrix LS minimization, only the positional parameters included in the defined block were refined. The block contained exclusively atoms belonging to the cofactors, while all protein atoms were held at fixed refined positions.

These estimated bond distance error values are summarized in Table 3 and in Figs. 3, 4, 5 for all bonds within the cofactor molecules. They are one order of magnitude higher than usual for small molecules [33].

Fourier termination effects on the Mo site

The quality of the final model may be restricted by Fourier ripples at resolutions above 1 Å. This may shift the positions of atoms on the vicinity of strongly scattering atoms, usually metal ions and their ligands, which is of particular interest in metalloproteins [34]. Possible Fourier ripple effects were calculated mainly to determine changes in the Mo-H_2O/OH bond distances.

Starting with the final refined atomic model, two F_c maps were calculated in the vicinity of the Mo atom, with data truncated at 1.28 Å and 0.5 Å, respectively. The 0.5 Å map is virtually free from the Fourier ripples and the comparison between the two maps allows the estimation of a correction to be applied on each one of the Mo ligands positions. The differences between the two maps are minimal and within the experimental error, when calculated with the observed B_{eq} factor (*B*-factor equivalent to a set of ADPs) of 17.5 Å^2 for the Mo atom. On lowering the value for the B_{eq} of Mo to 5 Å^2 the effect of this artefact is enhanced, but even here calculated corrections were small (Mo-OH differs by 0.08 Å).

Refined MOP model

MOP is a globular shaped protein with a 75 Å average diameter, with a single polypeptide chain of 907 amino acid residues folded as a four-domain structure. Each of the first two domains, named FeS_II (distal) [plant-type ferredoxin (Fd) fold] and FeS_I (proximal) (four-helical fold, new for Fd), enclose the two [2Fe-2S] clusters, while the larger following domains, Mo1 and Mo2, anchor and stabilize the extended conformation of the pyranopterin cofactor [11] (Fig. 1). The current model is very well ordered, especially in hydrophobic and core regions of the molecule, as indicated by an overall *B*-factor of 24.7 Å^2 and by an estimated average error on the coordinates of 0.10 Å [35]. A few external and solvent-exposed loops suffer from a variable amount of disorder. The exposed loop connecting domains FeS_I and Mo1, between residues 168 and 172, is the most disordered region of the molecule and the site of insertion of the FAD domain present in the larger XO structure.

The r.m.s.d. between 904 C_α atoms of the two models (the former model refined at 1.8 Å [13] and the current one at 1.28 Å) is 0.26 Å. The improvement of the new model is reflected particularly in much clearer electron density maps for most of the molecule, especially in poorly ordered surface residues. Alternate conformations for 17 side chains and one main chain were clearly identified, having a shared associated occupancy ranging from 0.2–0.8 to 0.5–0.5 as described in Table 4. Con-

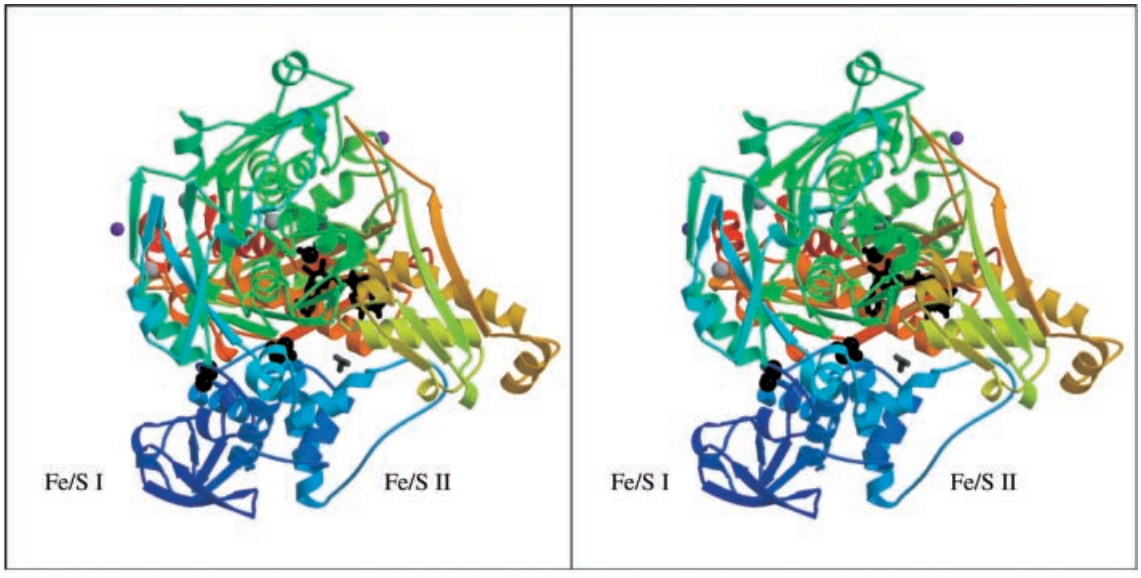

Fig. 1 Stereo view of the protein folding represented in a colour gradient from the N-terminus (*dark blue*) to the C-terminus (*red*). The [2Fe-2S] and MCD cofactors are shown in *black* and the two isopropanol molecules in *dark grey*. The Cl^- ions are represented as *light grey spheres* and Mg^{2+} ions, on the surface, as *purple spheres*. Figure built with Molscript [43] and Raster3D [44]

formational flexibility affects several exposed side chains where the electron densities vanish to a variable degree.

Two isopropanol (IPP) molecules from the crystallizing solution are present in the model; IPP1 is in the second coordination sphere of the molybdenum acting as an inhibitor, in agreement with our earlier studies, which provided the basis for the enzymatic mechanism when taking a Michaelis complex as a model [13]. A second isopropanol molecule, IPP2, is on the external surface of the protein molecule, on its first hydrating shell, and is H-bonded to water molecules.

Mg^{2+} and Cl^- ions in the crystal packing

As described in Materials and methods, the salts $MgCl_2$ or $CaCl_2$ were essential for the crystallization of MOP and the same crystal form was always obtained either when using different combinations of alcohols or when slightly changing the pH.

At later stages of refinement, Cl^- and Mg^{2+} ions from the crystallization solution were clearly identified on F_o–F_c electron density maps over 4σ levels (2.43 e Å^{-3}). As depicted in Fig. 1, three Cl^- and two Mg^{2+} ions were included in the final model and, with the exception of Cl1, which is rather buried, all others are close to the molecular surface, some favouring and stabilizing crystal contacts.

One of the Cl^- ions, Cl1, is located in an internal pocket, filled with four water molecules, which form a water chain directed towards the isopropanol molecule of the active site. The distance from Cl1 to the Mo atom is 8.2 Å. It is stabilized by the vicinity of a positively charged residue, Arg460, only 3.4 Å away. This Arg460 is conserved in the XO family. In the homologous enzyme MOD [16], where the crystallization conditions were different, Cl1 is replaced by a water molecule.

As depicted in Fig. 2, in the first hydration shell, Mg1 and Cl3 make protein symmetry contacts that constitute a strong intermolecular contact and contribute to the molecular packing. Mg1 makes two ionic contacts to Glu899 Oϵ2 and to Glu903 Oϵ1 and to the symmetry related Asp263 Oϵ1. Three water molecules complete the coordination sphere of Mg1, which displays octahedral geometry. The carboxylate of Glu899 makes a salt bridge with Lys248 from a symmetry mate (the distance Glu899 Oϵ1-Nϵ Lys248 is 2.74 Å). Chloride Cl3, which is only 2.99 Å away from Nϵ of Lys248, completes a network of electrostatic interactions at the crystal contact, possibly due to the presence of Mg^{2+} and Cl^- ions.

Table 4 Relative occupancy of the alternate conformations

Residue	Occupancy 1	Occupancy 2	Residue	Occupancy 1	Occupancy 2
Ile2	0.64	0.36	Leu410	0.53	0.47
Ala18	0.52	0.48	Glu561	0.78	0.22
Gln44	0.26	0.74	Cys661	0.74	0.26
Met233	0.52	0.48	Asp736	0.69	0.31
Ile240	0.52	0.48	Thr742	0.54	0.46
Ile322	0.48	0.52	Asn744	0.42	0.68
Asp379	0.68	0.32	Val834	0.49	0.51
Leu396	0.56	0.44	Leu872	0.63	0.37
			Lys828-CO	0.58	0.42

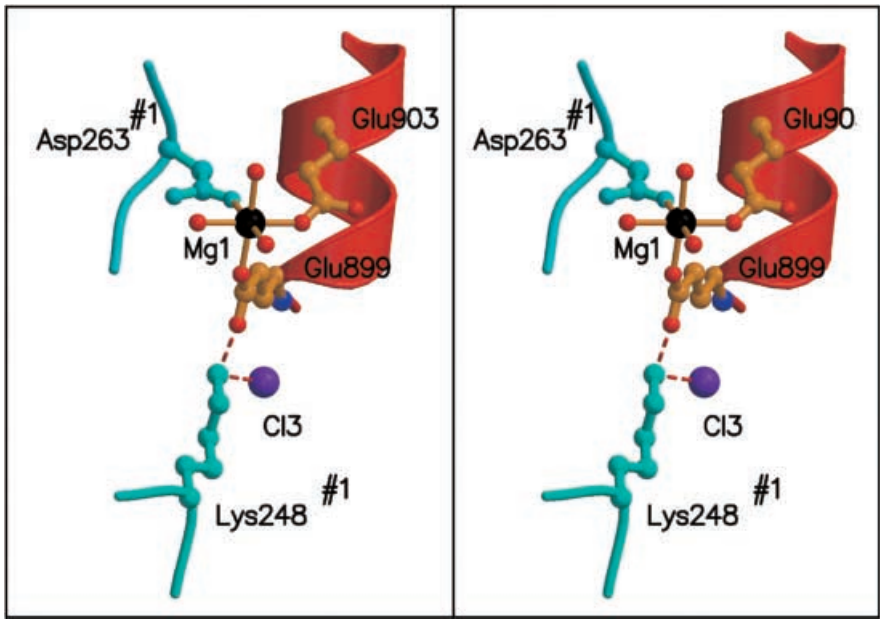

Fig. 2 Stereo representation of the crystal packing contacts around one of the Mg^{2+} ions, Mg1 (*black*). It shows octahedral coordination geometry to three water molecules, to Glu899 Oϵ2 and Glu903 Oϵ1 from the C-terminus helix (*red*) and to Asp263 Oϵ1 from a symmetry mate 1 (*blue*). Glu899 Oϵ1 establishes a salt bridge to Lys248 Nϵ, which is 2.99 Å from Cl3. Figure prepared with Molscript [43] and Raster3D [44])

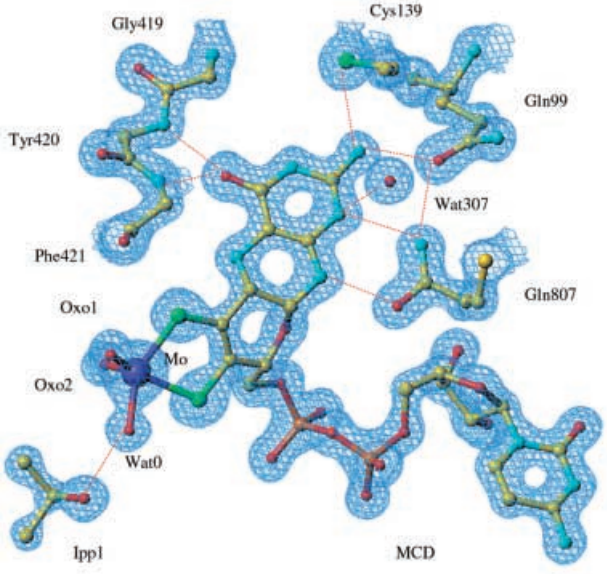

a)

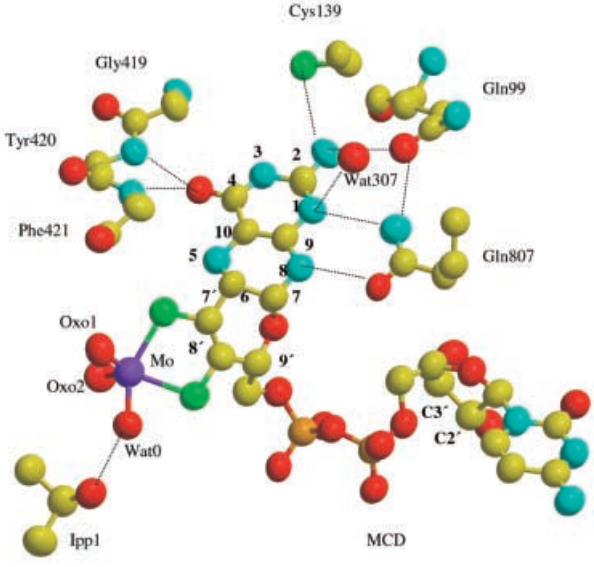

b)

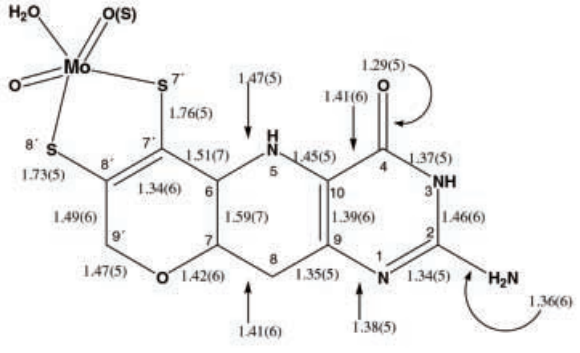

c)

	Oxo1	Wat0	Oxo2	MCD-S7′	MCD-S8′
Mo	1.74(4)	2.00(4)	1.79(4)	2.41(2)	2.50(2)

Other salt ions were recognized on the surface, such as an additional Cl^- ion, Cl2, found near the C-terminus and relatively close to positively charged residues, Lys900 (5.4 Å away) and Arg 893 (7.1 Å away). A second Mg^{2+} ion is also located at the molecular surface, far from crystal contacts. It defines a perfect octahedron with a cluster of water molecules as ligands. This cluster is found in a rather hydrophilic cavity, filled with 15 well-ordered water molecules which establish a network of hydrogen bonds among themselves and also to polar residues, which coat this exposed pocket, Asn511, Asp572, Arg569, Lys565 and Asp474.

The MCD cofactor

The chemical nature of the pterin cofactor had been suggested by Rajagopalan [36], with a pterin ring substituted at position 6 with a phosphorylated dihydropterin side chain containing a *cis* dithiolene bond. This model was confirmed and refined with the crystal structures of the W AOR from *P. furiosus* [9] and MOP [11]. In MOP, as in almost all bacterial enzymes, the tricyclic pyranopterin cofactor occurs as a dinucleotide. The MCD cofactor is buried 7 Å deep inside the protein, at the interface between Mo1 and Mo2, with a 15 Å deep hydrophobic tunnel allowing the access of substrate molecules to the catalytic site.

The MCD is subdivided in three parts: the cytosine dinucleotide which has the pyrimidine base in *anti* conformation and the D-ribofuranose sugar twisted with C2″ *endo* and C3″ *exo*; the pyrophosphate, which assumes different conformations in known enzyme structures; the tricyclic pyranopterin-ene-1,2-dithiolate, formed by a bicyclic pterin fused to a pyran ring, where the pterin system and pyran ring enclose an angle of about 28°. The pyrazine part of the system is twisted, with C6 *exo* and C7 *endo* being 0.4 Å and 0.3 Å apart from the reference plane, respectively, and the pyran ring is in an envelope conformation with O9′ *endo*.

The pyranopterin system is in the tetrahydropterin form. Protonation at C6 and C7 is in agreement with tetrahedral geometry with bond angles ranging from 107° to 114°. Furthermore, the C6-C7 single bond is 1.59(6) Å, approximately 0.20 Å longer than the C9-C10 double bond. N5 and N8 are probably also protonated, as the N5-C6 and N5-C10 distances and the N8-C9 distance are equal or larger than the database-derived target values for bonds with protonated N atoms.

◀

Fig. 3a–c Representation of the MCD cofactor and main contacts of the pyranopterin moiety with the surrounding protein residues. **a** The final atomic model with the 1.6σ (0.97 e Å^{-3}) $2F_o$–F_c electron density map superimposed. **b** Representation of the anisotropic atomic model, with the ellipsoids contoured to enclose a probability of 35%. **c** Schematic representation of Moco with bond distances including errors in parentheses. Parts **a** and **b** were prepared with TURBO-FRODO [28], Molscript [43] and Raster3D [44]

The pterin ring is stabilized on one side by Phe421 and Tyr420 via the carbonyl O4 atom pair of hydrogen bonds, whilst on the other side H-bonds are made from the amino group NH_2 to the Sγ of Cys139 and to the carbonyl Oϵ of Gln99. The N1 edge is H-bonded to the Nδ1 amine side-chain group of Gln807 and to a water molecule. The last H-bond interaction from the tricyclic pterin belongs to the pyrazine ring from the N8 edge to the Oϵ1 of Gln807 (Fig. 3). Other MCD contacts have been described elsewhere [37].

The Mo active site

Mo is present in the oxidized form and is penta-coordinated by two dithiolene sulfurs and three oxygen ligands. The *cis* dithiolene group and the molybdenum atom form the equatorial plane of the metal ligands, with covalent bonds of 2.41(2) Å to S7′ and 2.50(2) Å to S8′. The molybdenum atom is further coordinated at a distance of 1.77(4) Å to the apical oxo ligand, 1.79(4) Å to the basal oxo ligand and 2.02(4) Å to the water molecule. These values confirm the 1.8 Å resolution results for the desulfo-oxidized form of the enzyme [13], interpreted with two oxo and one water ligand.

The [2Fe-2S] clusters I and II

Two inorganic one-electron redox [2Fe-2S] centres contact the MCD cofactor, and their role consists in transferring electrons out of the buried MCD to the external surface, and from there to an electron acceptor. As the reaction mechanism consists of a coupled pair of reductive and oxidative half-reactions, characterized by reduction of Mo(VI) and oxidation of Mo(IV) [13], molybdenum has to be restored to the resting Mo(VI) state through a two-step sequence of one-electron transfers by the iron-sulfur clusters, generating the intermediate Mo(V) state.

The Fe/S centre proximal to Mo (centre I) (four-helical fold domain) is buried ca. 15 Å from the nearest surface, with a distance of 15 Å to the active site (Fe1···Mo). The distal Fe/S cluster (centre II) has a typical plant-type Fd coordination motif, is near the molecular surface, and 12.2 Å (FeS-I, Fe2-Fe1, FeS-II) from cluster I. The clusters were recently assigned for MOP [38] as well as for the homologous enzyme from *D. alaskensis* [39] on the basis of the anisotropy of their EPR signals (*g*-tensor). Accordingly, the centre of type I with the lower anisotropy is the proximal Fe/S centre, while the distal, plant-type Fe/S cluster, with a higher anisotropy, is FeS_II. The redox potentials are –260 mV and –285 mV for centres I and II, respectively [40].

In Figs. 4 and 5 are depicted both [2Fe-2S] clusters, superimposed on the final electron density map, contoured at 1.8σ, as well as the anisotropy model. The

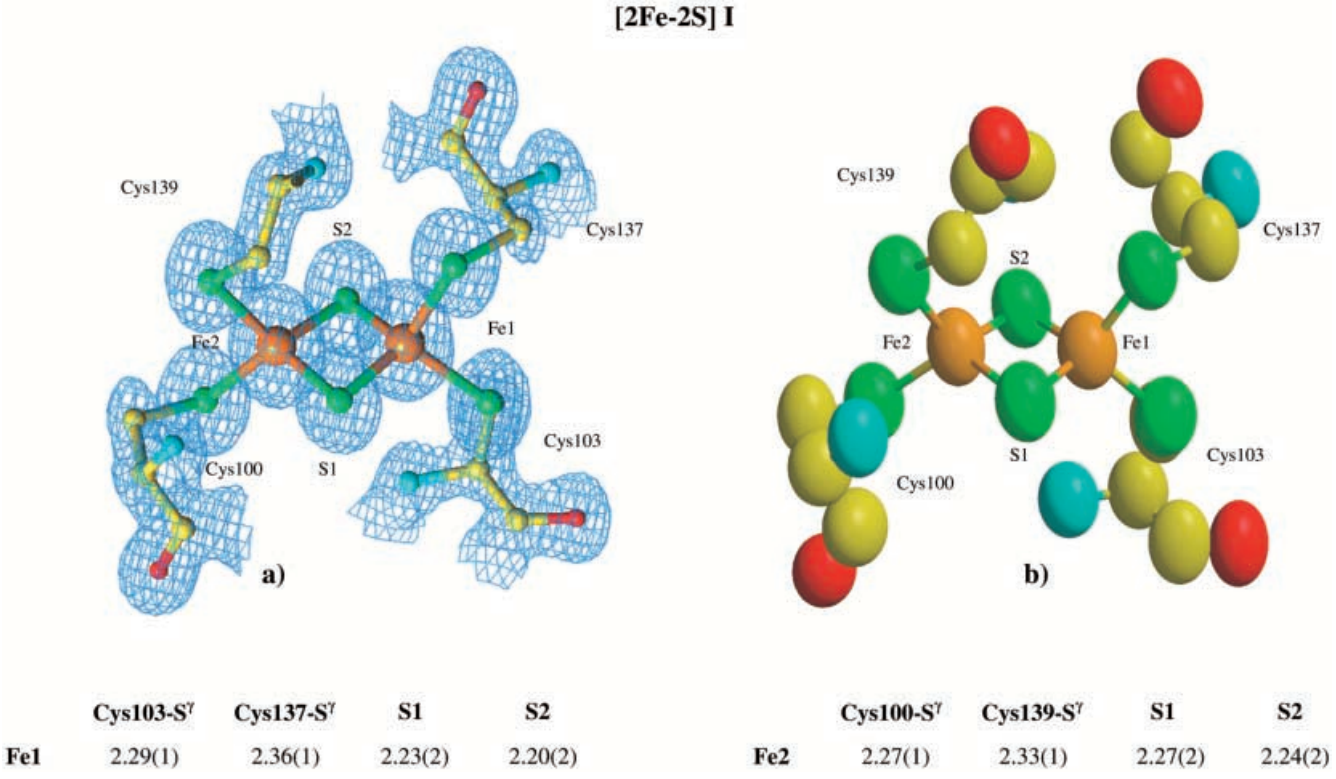

	Cys103-S^{γ}	Cys137-S^{γ}	S1	S2
Fe1	2.29(1)	2.36(1)	2.23(2)	2.20(2)

	Cys100-S^{γ}	Cys139-S^{γ}	S1	S2
Fe2	2.27(1)	2.33(1)	2.27(2)	2.24(2)

Fig. 4a, b The atomic model of the proximal FeS_I cluster, from the four-helical domain and with the cysteinyl coordination Cys100-X_2-Cys103-X_n-Cys137-X_2-Cys139. **a** The final atomic model with the 1.8σ (1.09 e Å^{-3}) $2F_o$–F_c electron density map superimposed. **b** Anisotropic atomic model with the ellipsoids contoured for a 35% probability distribution. Bond distances include errors in parentheses. Parts **a** and **b** prepared with TURBO-FRODO [28], Molscript [43] and Raster3D [44]

FeS_I cluster is surrounded by seven N-H···S hydrogen bonds to cysteinyl S^{γ} and to inorganic S atoms, and one N-H···O to a water molecule, while cluster II establishes a total of nine N-H···S bonds plus one N-H···O to an internal water molecule (see Table 5). In both clusters the pattern of N-H···S^{γ} Cys bonds is rather asymmetrical, which may explain the differences in the Fe-S^{γ} bond lengths [2.27(1) = Fe-S^{γ} = 2.37(1)]. Cluster Fe/S_II, with a plant-type Fd fold, exhibits an NH···S hydrogen bonding pattern very similar to the one found in the [2Fe-2S] cluster from plant-type Fds, although only for one of the Fe atoms. For example, in FdI from the blue alga *Aphanothece sacrum* [41], the pattern around the Fe atom bound to Cys39 and Cys44 (Cys40 and Cys45 in MOP) is very similar to what is found around Fe2 in MOP (Table 5). The only exception is the interaction with the O^{γ} of Ser38 in *A. sacrum* FdI, which in MOP is replaced by a NH···O bond to a water molecule. In FdI the second iron atom has no NH···S bonds in its environment, while in MOP the Fe2 cysteinyl sulfur atoms make two NH···S bonds.

This asymmetry found in both Fe/S clusters may explain why one of the two iron atoms in [2Fe-2S] clusters is more easily reduced. Studies carried out with several ferredoxins showed a correlation of the number of NH···S bonds around each Fe centre with the redox potential, suggesting an increase of 75–80 mV per single NH···S bond [41, 42]. In cluster II, Fe2 is stabilized by a total of four NH···S^{γ} bonds, two more than around Fe1. On this basis one might expect that, in cluster II, Fe2 would be more easily reduced than Fe1.

The new atomic coordinates have been deposited in the Brookhaven Protein Structure Database with the accession code 1ALO.

Table 5 NH···S and OH···S hydrogen bonds established by [2Fe-2S] I and [2Fe-2S] II centres to neighbouring residues

Acceptor	Donor	Distance (Å)
[2Fe-2S] I (new four-helical fold)		
S^{γ} Cys100	HN Phe102	3.36
S^{γ} Cys139	H_2N MCD	3.14
S^{γ} Cys137	HN Tyr140	3.38
	HN Cys139	3.52
S1	HN Gly101	3.48
	HN Glu99	3.54
S2	HN Arg138	3.39
	H_2O Wat105	3.38
[2Fe-2S] II (plant-type Fd fold)		
S^{γ} Cys40	HN Gln44	3.33
	HN Gln42	3.18
S^{γ} Cys45	HN Ala47	3.37
	H_2O Wat200	3.63
S^{γ} Cys48	HN Cys60	3.40
S^{γ} Cys60	HN Gly43	3.49
S2	HN Gly39	3.24
	HN Glu41	3.42
S1	HN Cys45	3.33
	HN Gly46	3.25

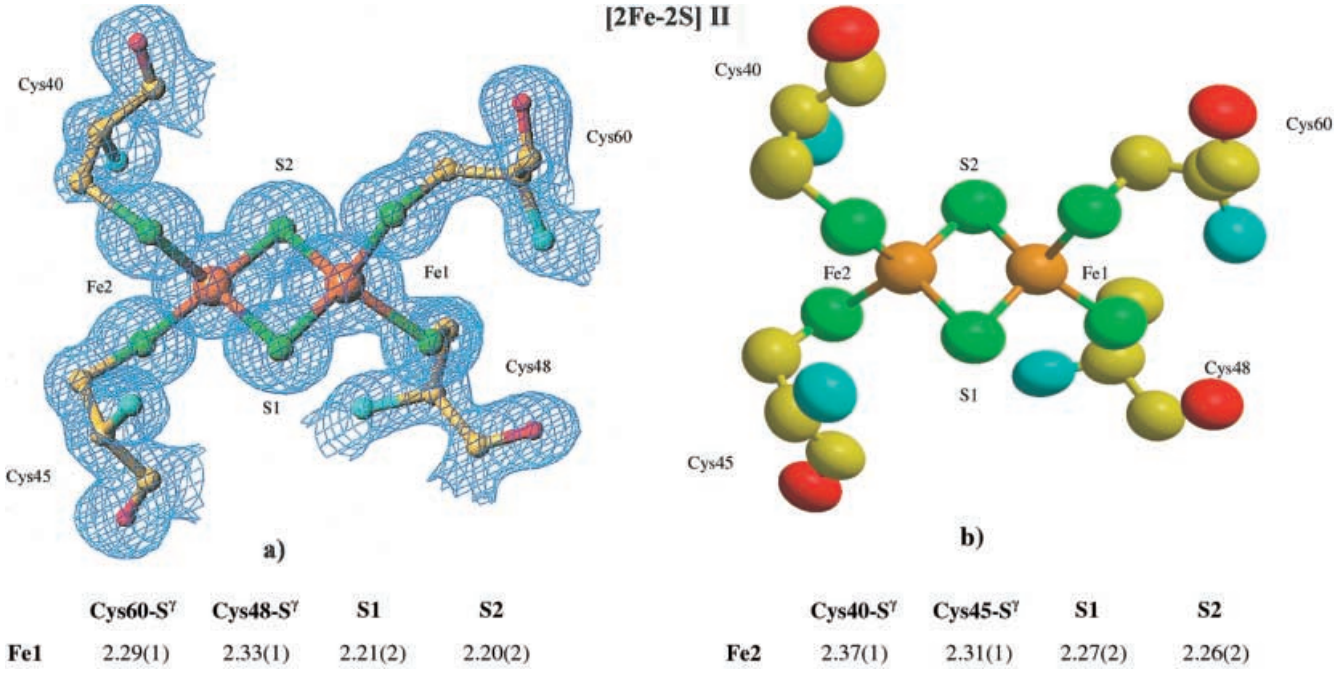

Fig. 5a, b The atomic model of the distal FeS_II cluster, with the plant-type ferredoxin fold and coordination motif Cys40-X_4-Cys45-X_2-Cys48-X_n-Cys60. **a** The final atomic model with the $2F_o$–F_c electron density maps drawn at 1.8σ (1.09 e Å^{-3}) superimposed. **b** Anisotropic atomic model for 35% probability distribution. Bond distances include errors in parentheses. Parts **a** and **b** prepared with TURBO-FRODO [28], Molscript [43] and Raster3D [44]

Acknowledgements This work was supported by EC-TMR/FMRX-CT980204, HPRN-CT-1999-00084, PhD grants PRAXISXXI/BD/13530/97 (J.M.D.) and PRAXISXXI/BD/21493/99 (J.R.). Hans Bartunik and Gleb Bourenkov are acknowledged for help at the BW6 beamline of the MPG-ASMB in DESY, Hamburg, Germany.

References

1. Stiefel EI (1997) J Chem Soc Dalton Trans 3915–3923
2. Hille R (1996) Chem Rev 96:2757–2816
3. Romão MJ, Knäblein J, Huber R, Moura JJG (1997) Prog Biophys Mol Biol 68:121–144
4. Dias JM, Than ME, Humm A, Huber R, Bourenkov GP, Bartunik HD, Bursakov S, Calvete J, Caldeira J, Carneiro C, Moura JJG, Moura I, Romão MJ (1999) Structure 7:65–79
5. McAlpine AS, McEwan AG, Shaw AL, Bailey S (1997) JBIC 2:690–701
6. Schindelin H, Kisker C, Hilton J, Rajagopalan KV, Rees DC (1996) Science 272:1615–1621
7. Schneider F, Löwe J, Huber R, Schindelin H, Kisker C, Knäblein J (1996) J Mol Biol 263:53–69
8. Kisker C, Schindelin H, Pacheco A, Wehbi WA, Garrett RM, Rajagopalan KV, Enemark JH, Rees DC (1997) Cell 91:973–983
9. Chan MK, Mukund S, Kletzin A, Adams MWW, Rees DC (1996) Science 267:1615–1621
10. Romão MJ, Barata BAS, Archer M, Lobeck L, Moura I, Carrondo MA, LeGall J, Lottspeich F, Huber R, Moura JJG (1993) Eur J Biochem 215:729–732
11. Romão MJ, Archer M, Moura I, Moura JJG, LeGall J, Engh R, Schneider M, Hof P, Huber R (1995) Science 270:1170–1176
12. Enroth C, Eger BT, Okamoto K, Nishino T, Nishino T, Pai EF (2000) Proc Natl Acad Sci USA 97:10723–10728
13. Huber R, Hof P, Duarte RO, Moura JJG, Moura I, Liu M, LeGall J, Hille R, Archer M, Romão MJ (1996) Proc Natl Acad Sci USA 93:8846–8851
14. Voityuk A, Albert K, Köstlmeier S, Nasluzov VA, Neyman KM, Hof P, Huber R, Romão MJ, Rösch N (1997) J Am Chem Soc 119:3159–3160
15. Voityuk A, Albert K, Romão MJ, Huber R, Rösch N (1998) Inorg Chem 37:176–180
16. Rebelo J, Macieira S, Dias JM, Huber R, Ascenso C, Rusnak F, Moura JJG, Moura I, Romão MJ (2000) J Mol Biol 297:135–146
17. Dunitz J, Schomacker V, Trueblood KN (1989) J Phys Chem 92:856–867
18. Merritt AM (1999) Acta Crystallogr Sect D 55:1997–2004
19. Moura JJG, Xavier AV, Brusci M, LeGall J, Hall D, Carmmack R (1976) Biochem Biophys Res Commun 72:782–789
20. Moura JJG, Xavier AV, Carmmack R, Hall D, Brusci M, LeGall J (1978) Biochem J 173:419–425
21. Otwinowski Z, Minor W (1993) DENZO: a film processing program for macro-molecular crystallography. Yale University Press, New Haven
22. Otwinowski Z, Minor W (1997) Methods Enzymol 276:307–326
23. CCP4 Collaborative Computational Project No 4 (1994) Acta Crystallogr Sect D 50:760–763
24. Matthews BW (1968) J Mol Biol 33:491–497
25. Brünger AT (1992) Nature 355:472–475
26. Brünger AT (1990) X-PLOR, version 3.851. Yale University Press, New Haven
27. Engh R, Huber R (1991) Acta Crystallogr Sect A 47:392–400
28. Roussel A, Cambillau C (1992) TURBO-FRODO molecular modelling package. In: Silicon Graphics geometry partner directory. Silicon Graphics, Mountain View, Calif., pp 77–78
29. Sheldrick G, Schneider T (1997) Methods Enzymol 277: 319–343
30. Tronrud DE (1992) Acta Crystallogr Sect A 48:912–916
31. Allen FH, Bellard S, Brice MD, Cartwright BA, Doubleday A, Higgs H, Hummelink T, Hummelink-Peters BG, Kennard O, Motherwell WDS, Rodgers JL, Watson DG (1979) Acta Crystallogr Sect B 35:2331–2339
32. Laskowski RA, McArthur MW, Moss DS, Thornton DS (1993) J Appl Crystalogr 26:283–291

33. EU 3-D Validation Network (1998) J Mol Biol 276:417–436
34. Schindelin H, Kisker C, Rees DC (1998) JBIC 2:773–781
35. Luzatti PV (1952) Acta Crystallogr Sect D 5:802–810
36. Rajagopalan KV (1991) Adv Enzymol 64:215–290
37. Romão MJ, Huber R (1998) Struct Bonding 90:69–96
38. Caldeira J, Belle V, Asso M, Guigliarrelli B, Moura I, Moura JJG, Bertrand P (2000) Biochemistry 39:2700–2707
39. Andrade SLA, Brondino C, Feio MJ, Moura I, Moura JJG (2000) Eur J Biochem 267:2054–2061
40. Moura JJG, Xavier AV, Cammack R, Hall DO, Bruschi M, LeGall J (1978) Biochem J 173:419–425
41. Tsukihara T, Fukuyama K, Mizushima M, Harioka T, Kusunoki M, Katsube Y, Hase T, Matsubara H (1990) J Mol Biol 216:399–410
42. Carter CW (1997) J Biol Chem 252:7802–7811
43. Kraulis PJ (1991) J Appl Crystallogr 24:946–950
44. Merrit EA, Murphy MEP (1994) Acta Crystallogr Sect D 50:869–873